

1 **New flow relaxation mechanism explains scour fields at the end of**  
2 **submarine channels**

3

4 **Authors**

5 F. Pohl,<sup>1\*</sup> J. T. Eggenhuisen,<sup>1</sup> M. Tilston,<sup>1</sup> M. J. B. Cartigny,<sup>2</sup>

6

7 **Affiliations**

8 <sup>1</sup> Faculty of Geosciences, Utrecht University, P.O. box 80021, 3508 TA Utrecht, The

9 Netherlands

10 <sup>2</sup> Department of Geography, Durham University, Lower Mountjoy South Road, DH1 3LE,

11 Durham, UK

12

13 \*Corresponding author: (florian.pohl63@gmail.com)

14 **Abstract**

15 In the ocean, particle-laden gravity flows, turbidity currents, flow in river-like channels across  
16 the ocean floor. These submarine channels funnel sediment, nutrients, pollutants and organic  
17 carbon into the ocean basins and can extend over 1,000's of kilometers. At the end of these  
18 channels, turbidity currents lose their confinement, decelerate and deposit their sediment load.  
19 This is what we read in textbooks. However, sea-floor observations have shown exactly the  
20 opposite: turbidity currents are prone to eroding the seafloor upon losing confinement. Such  
21 erosion features are commonly linked to a rapid flow transition associated with a hydraulic  
22 jump. This hypothesis has not been validated due to a lack of field measurements and scaling  
23 problems that prevented erosional turbidity currents to form in physical experiments. Here we  
24 use a state-of-the-art scaling method to produce the first experimental turbidity currents that  
25 erode upon leaving a channel. The experiments reveal a novel flow mechanism, here called  
26 'flow relaxation' that explains the erosion. Flow relaxation is the rapid, internal flow  
27 deformation resulting from the loss of confinement, which enhances basal shearing of the  
28 turbidity current, thus promoting local scouring. This flow mechanism provides a new  
29 explanation of scour formation at the end of channels and its role in the propagation of  
30 submarine channel systems.

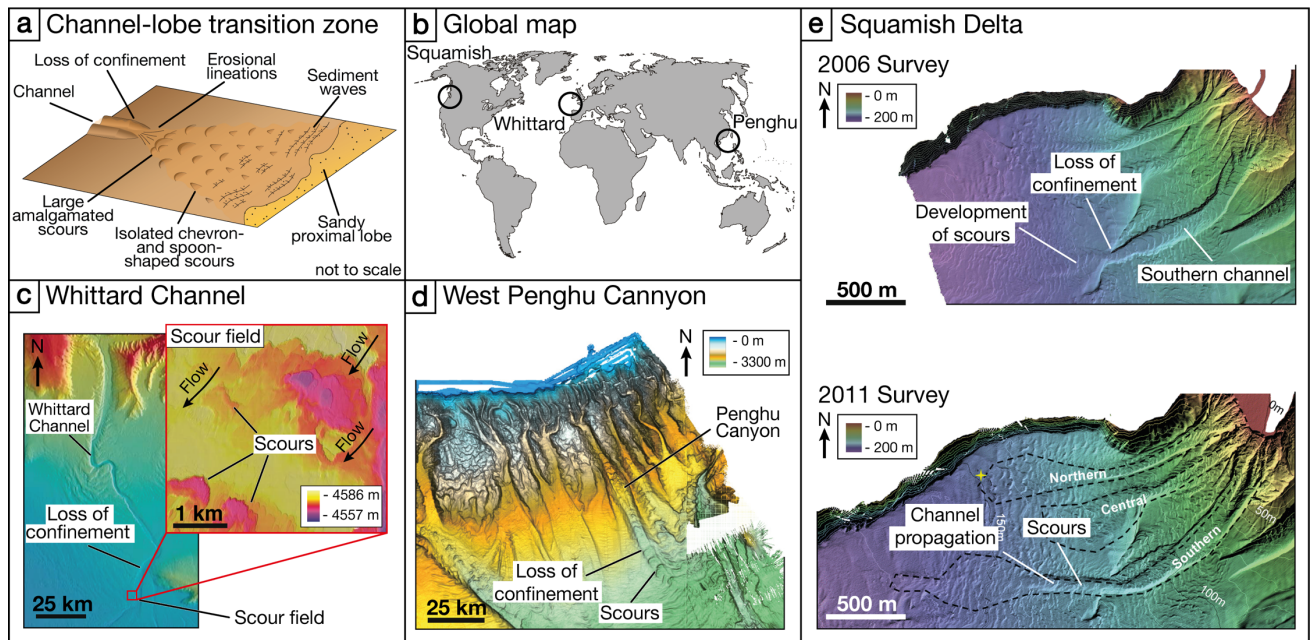
## 31 **Introduction**

32 Turbidity currents are particle-laden gravity flows that move downslope because of the  
33 density difference between the sediment-laden flow and the ambient water. They represent a  
34 major transport agent for sediment in the ocean, and turbidite deposits serve as a sink for  
35 organic carbon burial <sup>1,2</sup>, as major reservoirs for hydrocarbons <sup>3</sup>, and also as a depot for plastic  
36 debris <sup>4,5</sup>. On the ocean floor, turbidity currents typically transport sediment within  
37 confinements such as channels, which focus the flow and prevent deposition of the suspended  
38 sediment <sup>6</sup>. Upon leaving the channels, turbidity currents lose their lateral confinement and  
39 deposit their sediment load in lobate sediment bodies, forming the largest sediment  
40 accumulations on Earth <sup>7</sup>. While the sediment transport in channels and the deposition on  
41 lobes is reasonably well understood, it is not clear why these two systems are connected by a  
42 transition zone characterized by enhanced erosion, referred to as the channel-lobe transition  
43 zone (CLTZ) (Fig. 1a) <sup>8</sup>.

44 It is surprising that the area downstream of a channel is marked by erosion. The lateral  
45 expansion and associated deceleration of turbidity currents upon leaving the channel would  
46 suggest deposition. Previous research has established that a turbidity current leaving a channel  
47 confinement spreads laterally, and that lateral spreading increases the overall friction of the  
48 flow, resulting in deceleration and deposition of suspended sediment <sup>9,10</sup>. Yet bathymetric  
49 surveys on modern CLTZs show repetitive erosive structures, so-called scour fields, instead  
50 of the anticipated deposits (Fig. 1a) <sup>11-15</sup>. These scour fields can be >100 km long with  
51 individual scours up to 20 m deep and 2,500 m long (Fig. 1c) <sup>12,14</sup>. Erosion of the ocean floor  
52 at the CLTZ inherently plays a critical role in the development and the propagation of channel  
53 systems (Figs. 1d and e) <sup>16-20</sup>. Although erosive features of CLTZs are well documented, the  
54 dominant conceptual model to explain their genesis remains speculative and has not been  
55 subjected to rigorous experimental evaluation.

56 The favored hypothesis explaining erosion at the channel terminations is the occurrence of a  
57 hydraulic jump (i.e. the transition from Froude supercritical to Froude subcritical flow) as the  
58 turbidity current leaves the lateral confinement<sup>8,14,21</sup>. A hydraulic jump is expected to  
59 increase in the erosion potential of the flow, as turbulence in the flow is increased locally<sup>21-</sup>  
60<sup>23</sup>. Russell and Arnott<sup>24</sup> explain scouring in the CLTZ by the impingement of vortices that  
61 were produced by the hydraulic jump. However, there is no study that confirms the link  
62 between erosion processes and such hydraulic jump.

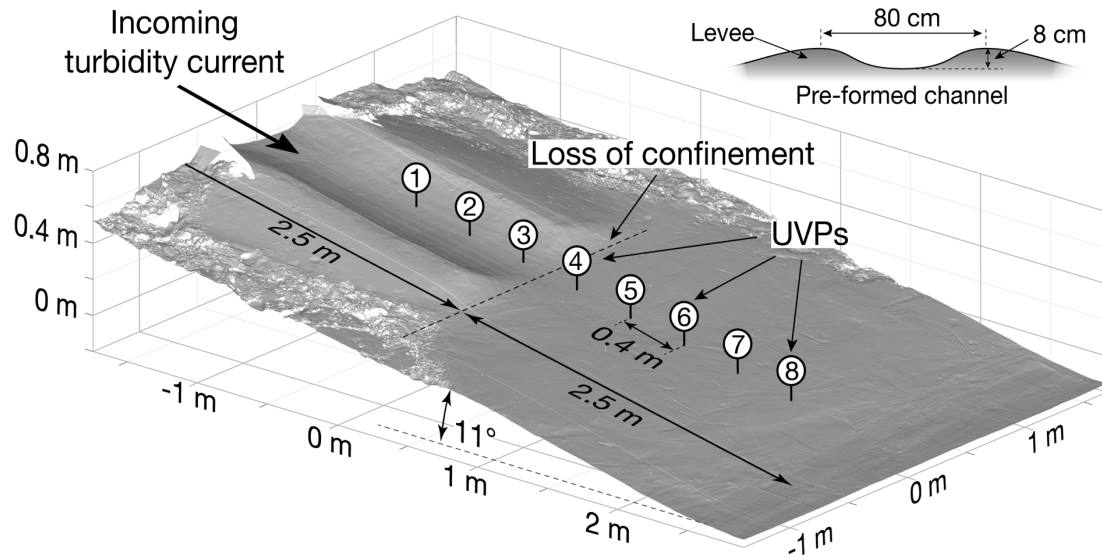
63 Here we use the newly developed Shields scaling approach<sup>25</sup> to directly observe the erosion  
64 mechanism in a turbidity current leaving a lateral confinement in an experiment set-up (Fig.  
65 2a). Additionally, we conduct a reference experiment in which the flow remained confined  
66 over the entire slope (Fig. 2b). The experiment method allows to observe the dynamic  
67 interaction between the turbidity current and the sea-floor in relation to the loss of  
68 confinement. The observed incision at the CLTZ is explained by a flow mechanism which we  
69 term ‘flow relaxation’. Flow relaxation results from the loss of lateral support of the turbidity  
70 current by the channel walls leading to a crucial mechanism for channel propagation on the  
71 ocean floor.



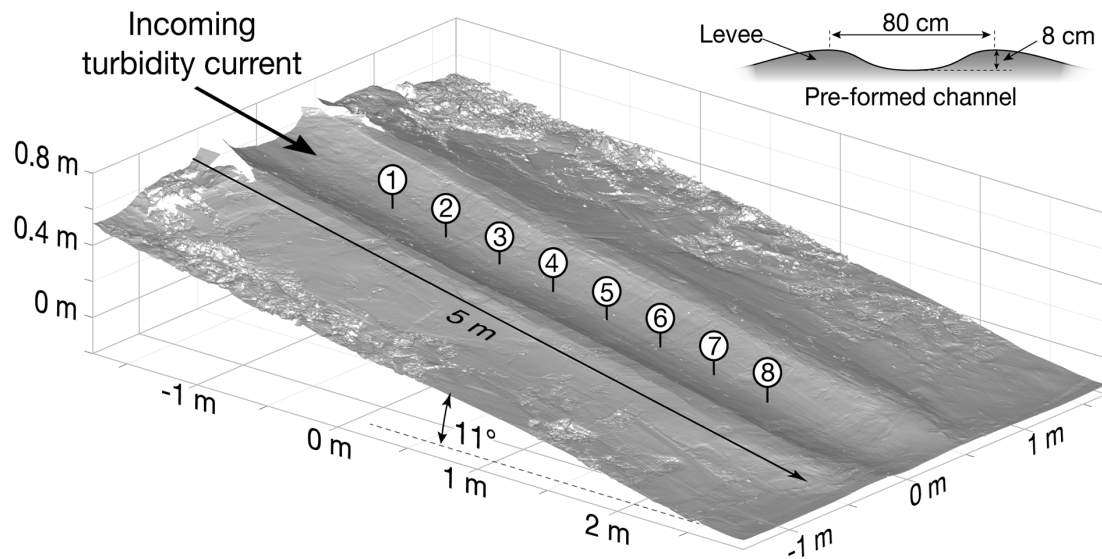
72

73 **Fig. 1. Examples of systems with a loss of confinement. a-e,** (a) Sketch of a channel-lobe  
 74 transition zone based on bathymetrical surveys. Modified from <sup>14</sup>. (b) Global map showing  
 75 the locations of the systems shown in panel c-e. (c) Bathymetry map of the Whittard Channel.  
 76 The ocean floor downstream of the channel termination is characterized by scour fields <sup>12</sup>. (d)  
 77 The West Penghu canyon in the South China Sea. Downstream of the loss of confinement the  
 78 ocean floor is marked by a line of scours indicating erosion and the progradation of the  
 79 canyon <sup>40</sup>. (e) The Squamish Delta. In the upper bathymetry map, the channel termination is  
 80 marked by a rapid loss of confinement <sup>39</sup>. The lower bathymetry map was obtained 5 years  
 81 later and shows how erosion has led the propagation of the channel by ~400 m <sup>37</sup>.

**a** Loss of confinement (initial bathymetry)



**b** Reference experiment (initial bathymetry)



82

83 **Fig. 2. Digital-elevation-models of the initial bathymetry. a,b,** (a) The experiment with  
84 loss of confinement. The loss of confinement was generated by a decrease of the levee height  
85 2.5 m downstream of the inlet box. (b) The reference experiment with a continuous pre-  
86 formed channel over the entire length of the slope. The substrate in both experiments was  
87 equivalent to that of the sediment mixture used to generate the experiment currents. The  
88 channel dimensions, as well as the input conditions of the incoming turbidity current, were  
89 identical in both experiments. UVP: Ultrasonic Velocimetry Probe.

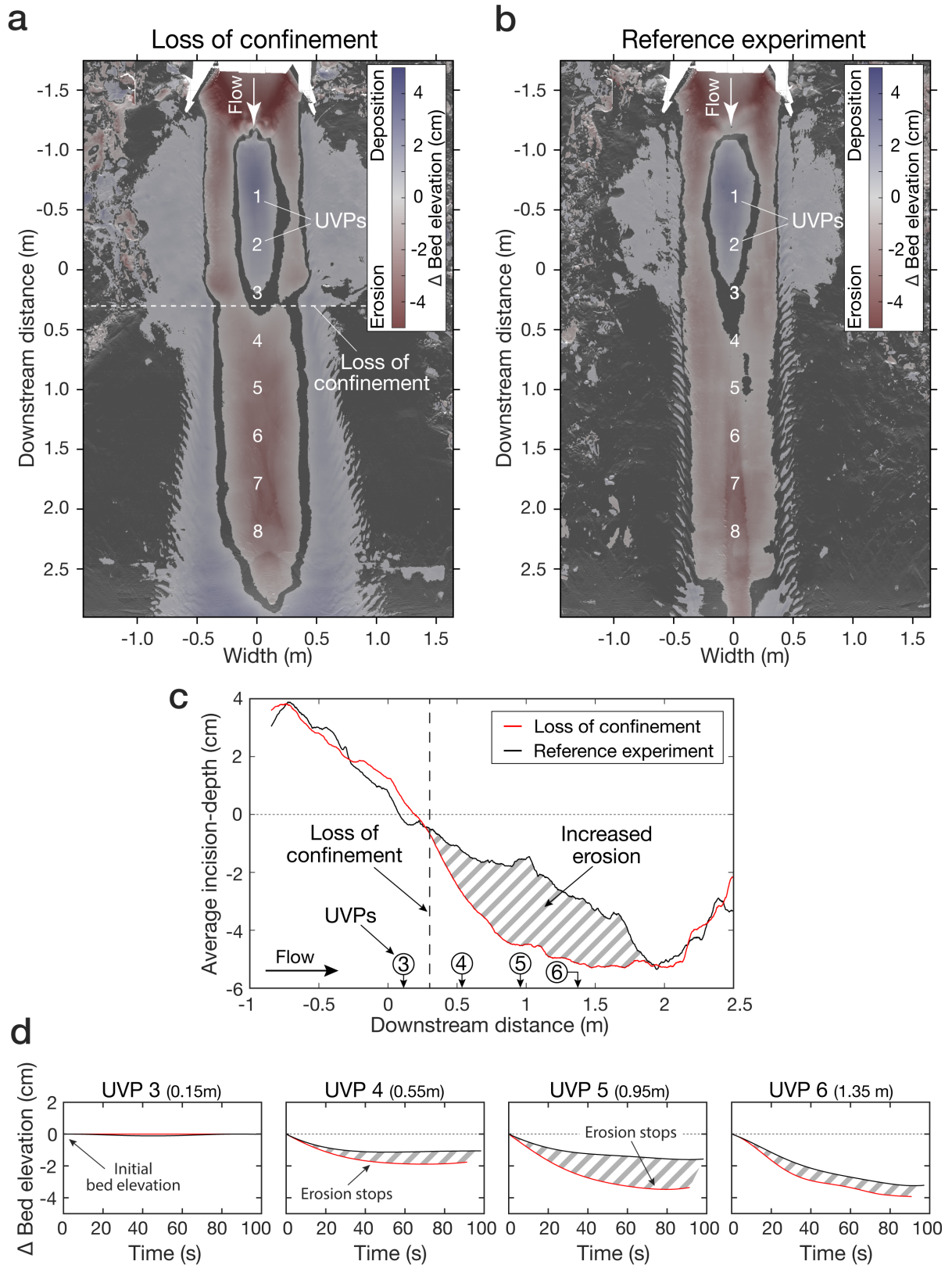
## 90 **Results**

91 The experiment results show the anticipated enhanced erosion downstream of the loss of  
92 confinement (Fig. 3a). Upstream of the loss of confinement both experiments display the  
93 expected similar behavior (Figs. 3a, b, and c). Upon losing confinement, however, the  
94 unconfined flow incised deeper along the down-flow trajectory than in the reference  
95 experiment without the loss of confinement. The incision in the center was flanked by  
96 deposition of a  $\sim 2$  cm high ridge on each side (Fig. 3a). In contrast, the reference experiment  
97 showed less incision and no depositional ridges (Fig. 3b). The overall morphologic  
98 development of incision flanked by depositional ridges generated a new confinement.  
99 The development of the self-confinement propagated downstream over time suggesting an  
100 association of enhanced erosion with incipient channel development. The propagation of the  
101 confinement was captured by the velocity probes (Fig. 3d). The enhanced erosion rate (i.e.  
102 change in bed elevation) decreased to zero at UVP 4 downstream of the loss of confinement  
103 over the first  $\sim 40$  s of the experiment (Fig. 3d), when the self-confinement was established.  
104 Further downstream, at UVP 5, the initial erosion rate decreased to zero over a longer time  
105 period of  $\sim 80$  s (Fig. 3d), implying a delayed establishment of the self-confinement at this  
106 location. Hence, the establishment and the propagation of the self-confinement in the  
107 experiment was driven by on-axis erosion and off-axis deposition downstream of the loss of  
108 confinement.

109 The turbidity current immediately spread and thinned upon leaving the confinement, resulting  
110 in an increased basal shearing and erosion potential of the flow. The velocity of the turbidity  
111 current was captured by 8 velocity probes aligned along the channel thalweg (Figs. 2a and b).  
112 Each of the probes collected a full vertical velocity profile of the flow (Figs. 4a and b). The  
113 turbidity current accelerated down the channel as it entered the setup. Downstream of the loss  
114 of confinement the flow decelerated (Fig. 4c). Deceleration was accompanied with a decrease  
115 in flow thickness due to lateral spreading upon leaving the channel (Fig. 4d). However, due to

116 the thinning of the flow, the velocity gradient at the flow base is increased (cf. Fig. 4a), which  
117 enhances the friction between the flow and the bed, i.e. the bed shear velocity (Fig. 4e). The  
118 increased shear velocity upon thinning of the flow is responsible for the enhanced erosion  
119 downstream of the loss of confinement.





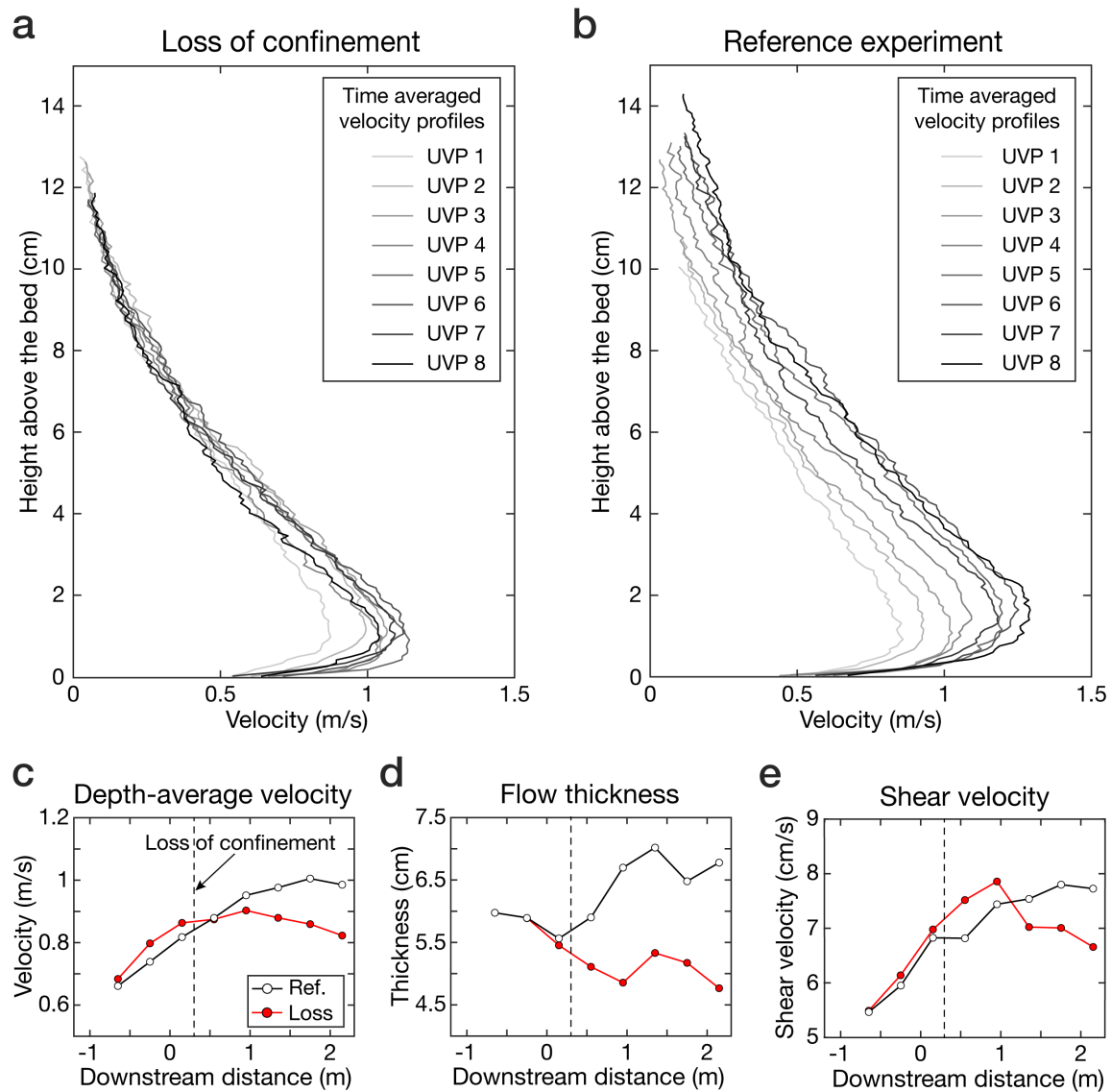
120

121 **Fig. 3. Erosion and deposition in the two experiments. a-d, (a),** Map showing erosion and

122 deposition in the experiment with the loss of confinement. **(b)** Erosion and deposition in the

123 reference experiment. **(c),** Laterally averaged incision-depth of a 30 cm wide strip along the

124 channel thalweg. Erosion in the experiment increased with the loss of confinement. **(d)**, Bed-  
125 elevation change during the experiments captured by the UVPs. Bed-elevation change was  
126 generally higher in the experiment with the loss of confinement than in the reference  
127 experiment. The difference was highest below UVP 5, which was located 0.95 m downstream  
128 of the loss of confinement.



129

130 **Fig. 4. Flow-dynamic parameters captured by the velocity probes. a-e, (a),** Time-averaged

131 velocity profiles for the turbidity current in the experiment with loss of confinement. **(b)**

132 Time-averaged velocity profiles for the turbidity current in the reference experiment (see

133 figure 2 and 3 for probe locations). **(c),** Depth-averaged velocity downstream of the loss of

134 confinement the turbidity current decelerated and was slower than the current in the reference

135 experiment. **(d),** Flow thickness. After leaving the confinement the turbidity current

136 immediately thinned. **(e),** Shear velocity. Shear velocity was slightly increased downstream of

137 the loss of confinement and decreased farther downstream.

## 138 **Discussion and conclusions**

139 As previously noted, the morphological changes at the loss of confinement result in rapid  
140 flow deformation, which in turn triggers enhanced erosion. Our results indicate that this  
141 deformation manifests itself through the vertical thinning and lateral spreading of the flow  
142 field. The mechanism leading to this transformation is explained through the concept of flow  
143 relaxation, which describes the reaction of the flow to the development of strong lateral  
144 pressure gradients upon exiting the channel (Figs. 5a and b).

145 We propose that changes in the lateral pressure gradient at the base of the flow explain the  
146 concept of flow relaxation. Within turbidity currents, hydrostatic pressure is increased by the  
147 mass of the overlying suspended particles, and since particle concentration decreases from the  
148 bed to the top of the current, so does the pressure<sup>26</sup>. The lateral pressure gradient is zero in a  
149 channelized flow, due to the absence of horizontal density gradients (Fig. 5a)<sup>27</sup>. When the  
150 flow loses confinement, a lateral pressure gradient develops between the dense current and the  
151 ambient fluid that drives flow spreading (Fig. 5b). The lateral pressure gradients are strongest  
152 at the bottom of the current, which explains the rapid basal evacuation and the lowering of the  
153 high velocity core. It is the lowering of this high velocity core that leads to an increase of the  
154 near-bed velocity gradient and bed shear velocity (Figs. 4a, d, and e), resulting in scour  
155 development. In this model the area between the proximal and distal regions of the scour field  
156 is interpreted as the distance over which the current re-equilibrates to the new unconfined  
157 flow conditions. In summary, rapid flow deformation and associated scour formation that  
158 occurs over this re-adjustment range is explained through changes in lateral pressure gradients  
159 as explained in the flow relaxation model (Figs. 5a and b).

160 Research to date has tended to ascribe the formation of scour fields in CLTZs to hydraulic  
161 jumps<sup>8,14,15,21,28,29</sup>. In this model scours would form because of enhanced turbulence created  
162 by a hydraulic jump<sup>21-23</sup>. In our experiments, we did not observe a hydraulic jump as the flow  
163 is thinning upon leaving the confinement (Fig. 4d), while a hydraulic jump would result in

164 thickening of the flow <sup>29</sup>. Previous experiments in saline density flows without suspended  
165 particle have observed a hydraulic jump at the channel termination <sup>20</sup>. However, this hydraulic  
166 jump was correlated with late-stage topographic forcing through channel mouth bar  
167 development rather than the loss of confinement. Moreover, a single hydraulic jump would  
168 form a single scour rather than scour fields as observed in CLTZs (Figs. 1a and c). Monitoring  
169 of saline flows in the Black Sea channel have revealed that each scour is associated with an  
170 individual hydraulic jump <sup>15,30</sup>. Consequently, Dorrell et al. <sup>15</sup> have evoked the presence of a  
171 ‘hydraulic-jump-array’ associated with the formation of a scour field in CLTZs. However, the  
172 density structure of the Black Sea saline flows is different from the density structure of a  
173 turbidity current <sup>31–33</sup>, and therefore it remains questionable whether such hydraulic-jump-  
174 array model translates across to turbidity currents. Furthermore, the hydraulic jumps in the  
175 Black Sea formed within the confinement of a channel, rather than at the loss of confinement  
176 of the CLTZ <sup>15,30</sup>. Finally, a third model explains multiple scours by the impingement of  
177 vortices into the ocean floor beneath a hydraulic jump <sup>24</sup>. In this model, each individual  
178 impingement would form a scour. However, scour formation by impingement of vortices was  
179 never produced in experiments. Overall, the association of scour fields in CLTZs with  
180 hydraulic jumps remains open for debate.

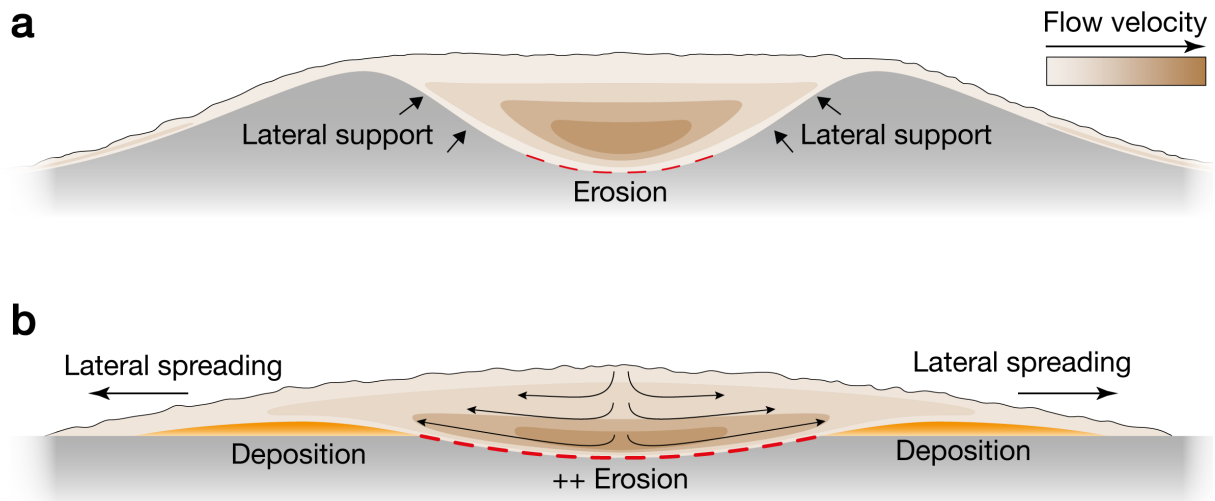
181 Flow relaxation is a mechanism that well explains the formation of scour fields in CLTZs.  
182 Instead of going through a hydraulic jump, the flow relaxes upon leaving the confinement,  
183 enhancing the basal shearing of the turbidity current (Figs. 4a and e). This increases the  
184 erosion of the sediment bed by the flow, and triggers scour formation <sup>34</sup>. Hence, the likelihood  
185 of the formation of scours is increased over the entire area in which the flow relaxes. In this  
186 area, the locations of individual scours are likely determined by irregularities and  
187 inhomogeneities on the ocean floor <sup>34</sup>, thereby explaining the observed scour fields in CLTZs.  
188 Submarine channels can grow to extraordinary lengths, like the Northwest Atlantic Channel  
189 which extends over up to ~3,800 km <sup>35</sup>. Additionally, these submarine channels can propagate

190 at exceptional rates of up to ~500 m/yr in the Amazon system <sup>36</sup> or ~80 m/yr. in the much  
191 smaller Squamish system <sup>37</sup>. This rate suggests a very effective channel propagation  
192 mechanism. The nature of this propagation mechanism is much debated, where attention has  
193 so far focused on whether the propagation of submarine channels is dominantly due to erosion  
194 or deposition <sup>16-19,25,38</sup>. Hamilton's et al. <sup>20</sup> experimental saline density flows show an increase  
195 in the flow sediment transport capacity at channel mouth, and they proposed erosion as the  
196 impetus for sustained channel propagation. Our results provide the physical processes that  
197 drive the erosion and demonstrate the applicability of the processes in sediment-laden flows,  
198 such as turbidity currents. As the flow relaxes at the channel termination, it incises in the  
199 center and deposits levee-shaped sediment bodies off-axis to both sides, efficiently forming a  
200 self-confinement (Figs. 3a and 5b). The self-confinement provides lateral support to the flow,  
201 which results in a decrease of the lateral pressure gradient, and maintains the flow thickness.  
202 Hence, the self-confinement is damping the effect of the flow relaxation and thus the erosion  
203 potential of the flow. Self-confinement establishes until an equilibrium channel shape is  
204 reached, thereby extending the channel further across the ocean floor.

205 Our model provides a mechanism explaining the propagation of a channel in the Squamish  
206 ProDelta. A bathymetry map of the Squamish Delta that was monitored in 2006, showed that  
207 the Southern Channel terminated with a rapid loss of confinement (Fig. 1e) <sup>39</sup>. A subsequent  
208 bathymetry study in 2011 revealed propagation of the Southern Channel over a distance of  
209 ~400 m (Fig. 1e) <sup>37</sup>. Channel propagation was generated by incision into the underlying  
210 substrate downstream of the rapid loss of confinement and, hence, driven by erosion  
211 comparable to the channel propagation in our experiments (Fig. 3a).

212 Our results provide measurements of a turbidity current that enhances its erosion potential by  
213 leaving a channel. Upon leaving the channel confinement the turbidity current laterally  
214 spreads and thins, which causes an increase in the bed shear stress and erosion. The here  
215 introduced model of flow relaxation provides a flow dynamic process that is pivotal for the

216 development of scour fields in CLTZs, and plays a central role in the propagation of  
217 submarine channels.  
218



219  
220 **Fig. 5. Illustration of the flow relaxation model. a,b,** (a) Flow confined in a channel. The  
221 channel side-walls counteract the near-bank lateral pressure differences within the flow,  
222 resulting in a lateral pressure gradient of zero. Note lateral and vertical variations in the flow  
223 velocity field, after <sup>27</sup>. (b) A flow that ‘relaxes’ upon leaving a confinement. The loss of  
224 lateral support by the channel flanks results in a lateral pressure gradient within the flow, and  
225 hence, lateral spreading and thinning. This shifts the height of the maximum velocity bed-  
226 wards, increases the shear stress at the bed, resulting in erosion. Lateral to the incision, levee-  
227 shaped sediment bodies are deposited due to the lateral decrease in flow velocity.

## 228 **Materials and Methods**

229

### 230 **Scaling approach**

231 The turbidity currents were downscaled from natural to experiment size by using Shields  
232 scaling<sup>25</sup>. This technique relies on two scaling parameters: (1) The Shields parameter, which  
233 is kept close to natural values, and (2), the boundary Reynolds number, which is relaxed as  
234 long as rough to transitionally rough boundary layer conditions are maintained (Fig. S1).  
235 Together, these two parameters predict whether the current will erode or deposit sediments  
236 and whether the particles will be transported as bedload or suspended load.

237 The Shields parameter describes the ratio between the shear stress and the gravity force acting  
238 on particles<sup>41</sup>:

$$239 \quad \theta = \frac{\rho_t u_*^2}{(\rho_s - \rho_w) g d_t}, \quad (1)$$

240 where  $\rho_s$  is the density of the suspended sediment (quartz sand with 2650 kg/m<sup>3</sup>),  $\rho_w$  the  
241 density of water (1000 kg/m<sup>3</sup>),  $d_t$  the grain size of the suspended sediment,  $g$  the gravitational  
242 force (9.81 m/s<sup>2</sup>), and  $u_*$  the shear velocity (Eq. 3). The density of the turbidity current  $\rho_t$  is:

$$243 \quad \rho_t = (\rho_s - \rho_w) C + \rho_w, \quad (2)$$

244 with  $C$  as the sediment concentration. The shear velocity  $u_*$  can be derived from the shape of  
245 the velocity profile below the velocity maximum  $U_{max}$ , by assuming a logarithmic velocity  
246 profile between the bed and the height of the velocity maximum  $h_m$ <sup>25,42-44</sup>:

$$247 \quad u_* = U_{max} \kappa \left( \ln \left( \frac{h_m}{0.1 d_{90}} \right) \right)^{-1}, \quad (3)$$

248 where  $\kappa$  is the von Kármán constant with a value of  $\sim 0.4$ . The  $d_{90}$  is derived from the grain-  
249 size distribution in the turbidity current.



250 Studies of natural turbidity currents revealed a typical value for the Shields parameter of 1 –  
251 10 (Fig. S1)<sup>2,45</sup>. In our experiments, we meet these values by varying the sediment  
252 concentration and the velocity of the flow by varying the slope accordingly.  
253 The boundary Reynolds number  $Re_p$  controls the hydraulic conditions of the viscous sub-  
254 layer, from hydraulically smooth ( $Re_p < 5$ ), to transitional ( $5 < Re_p < 70$ ), to hydraulically  
255 rough ( $Re_p > 70$ )<sup>46</sup>. In the hydraulically rough regime, the viscous sub-layer is dominated by  
256 turbulent forces, whereas in a hydraulically smooth regime the viscous sub-layer is dominated  
257 by viscous forces. Studies report a transitionally rough regime for natural turbidity currents  
258 (Fig. S1)<sup>2,47</sup>. The value of the  $Re_p$  is given by the ratio of the grain size to the thickness of the  
259 viscous sub-layer:

$$Re_p = \frac{u_* d_b}{\nu}, \quad (4)$$

260  
261 where  $d_b$  is the grain size of the sediment of the bed, and  $\nu$  is the kinematic viscosity of clear  
262 water at 20°C ( $1 \times 10^{-6}$  m<sup>2</sup>/s). In the experiments, we meet the transitionally rough hydraulic  
263 regime by using a fine grain size ( $d_{10} = 35 \mu\text{m}$ ,  $d_{50} = 133 \mu\text{m}$ ,  $d_{90} = 214 \mu\text{m}$ ) for the sediment  
264 of the bed (Fig. S2). We also use the same grain size for the suspended sediment of the  
265 turbidity current to avoid changes in bed grain size due to deposition from the flow.

266

## 267 **Experiment setup and procedure**

268 The turbidity currents were released into a 11 m x 1.3 m x 6 m (length x height x width)  
269 basin, filled with fresh water (Fig. S3). The floor consists of a 5 m long slope of 11°, followed  
270 by a horizontal basin floor of 6 x 6 m at the base of slope (Fig. S3). The turbidity current was  
271 generated from a 0.9 m<sup>3</sup> mixture of sediment and water prepared in a separate mixing tank  
272 using quartz sand with a mean density of 2650 kg/m<sup>3</sup>, particle diameter ( $d_{50}$ ) 133  $\mu\text{m}$  (Fig.  
273 S2), and volumetric concentration of 17 %. The mixture was pumped into the basin with a  
274 radial-flow pump with a constant discharge of 30 m<sup>3</sup>/h. The discharge was monitored with an

275 electromagnetic flow-meter (Krohne Optiflux 2300) (Fig. S4). The turbidity current entered  
276 the setup at the upper end of the slope through an inlet box and flowed downslope driven by  
277 its excess density.

278 The initial bathymetry in the experiment consisted of an 11° sloping basin floor with a pre-  
279 formed channel that abruptly loses lateral confinement (Fig. 2a). The channel was formed by  
280 building confining levees on the slope, and the channel dimensions were 80 x 8 cm (width x  
281 depth). Both the levees and the slope were made of loose sand that had the same grain-size  
282 distribution as the sand used for the turbidity current (Fig. S2). During the experiment, the  
283 bulk portion of the flow was contained by the channel, with minimal overspill across the levee  
284 crests.

285 In a reference experiment, a pre-formed channel with identical dimensions was used, while  
286 the channel extended over the entire length of the sloping basin floor (Fig. 2b). Besides the  
287 difference in channel length, all other parameters were kept identical in the two experiments.

288

### 289 **Digital elevation model**

290 After the release of an experiment current, the basin was drained to expose the deposits. The  
291 deposits were scanned by a laser scanner with a measurement accuracy of <0.5 mm. From the  
292 laser scan a Digital Elevation Model (DEM) with a horizontal grid spacing of 2 x 2 mm was  
293 created. Subtraction of the post-flow DEM from the pre-flow DEM yields a map of the  
294 experiment current's deposition and erosion patterns (Figs. 3a and b).

295 To quantify the erosion during the two runs the average incision-depth was calculated (Fig.  
296 3c). Incision-depth was averaged along the width of a 0.3 m wide corridor, which was aligned  
297 within the channel thalweg along the downstream direction. Incision values were laterally  
298 averaged to remove "noise" associated with local variations in incision depth and therefore  
299 represent bulk-averaged trends.

300

### 301 **UVP data acquisition and processing**

302 An array of 8 Ultrasonic Velocimetry Profilers (UVPs) was installed along the channel axis to  
303 capture changes in the flow field associated with the abrupt loss of confinement (Figs. 2a and  
304 b); UVP acquisition settings are given in Table S1. The downstream spacing between  
305 individual UVPs was 0.4 m and the probes were set 0.15 m above the bed, facing the  
306 upstream direction at an angle of 60° with respect to the basin's initial bed configuration (Fig.  
307 S5a). Each UVP measures the velocity of sediment grains along the probe's axis, and the bed-  
308 parallel velocity component is obtained by trigonometric calculations (Fig. S5a); this  
309 calculation assumes that the bed-normal component of velocity is zero. The bed-parallel  
310 velocity against time for all UVPs is shown in figure S6 for experiment with the loss of  
311 confinement, and in figure S7 for the reference experiment. The interface between the flow  
312 and sediment bed was discernable as a sharp decrease in velocity (Figs. S6 and S7). The  
313 vertical bed position was tracked over time, yielding erosion and deposition rates below  
314 individual UVPs (Fig. 3d).

315 Time-averaged profiles were generated for the body of the current, where the flow is  
316 generally steady (Fig. 4a and b). The velocity measurement of the current head and of the tail  
317 were omitted for the time-averaging (Figs. S6 and S7). The time-averaged profiles were then  
318 smoothed using a Fournier fitting function to remove spurious spatial velocity fluctuations  
319 linked with the UVP's sampling resolution to determine the magnitude  $U_{max}$  and the height  $h_m$   
320 of the velocity maxima. The flow thickness  $h$  is defined here as the height at which the  
321 velocity  $u$  is half the velocity maximum  $U_{max}$  (Fig. S5)<sup>48-51</sup>. The depth-averaged velocity was  
322 averaged between the bed and the flow thickness  $h$ .

323

324 **Supplementary materials**

325 Fig. S1. Shields mobility diagram.

326 Fig. S2. Cumulative grain-size distribution.

327 Fig. S3. Schematic drawing of the experiment setup.

328 Fig. S4. Discharge measurements of the two experiments.

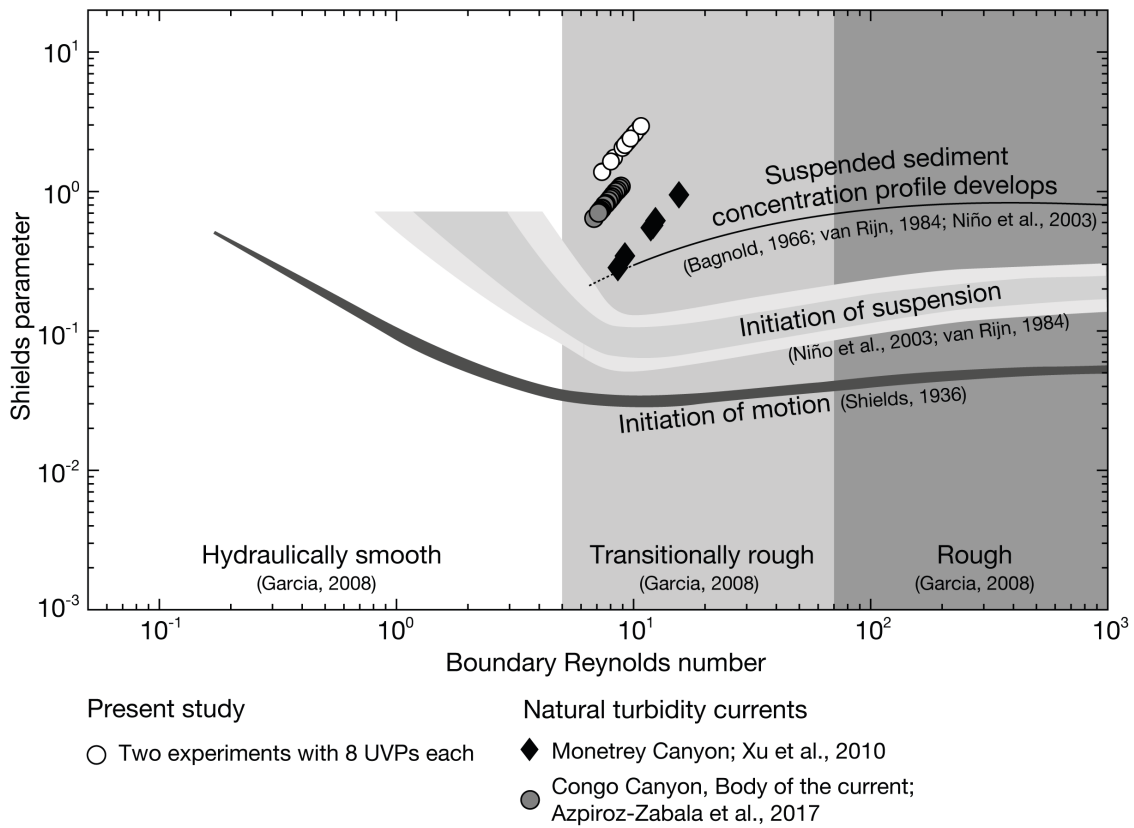
329 Table S1. UVP data acquisition settings.

330 Fig. S5. UVP orientation and parameterization of the velocity profile.

331 Fig. S6. Velocity measurements in the experiment with loss of confinement.

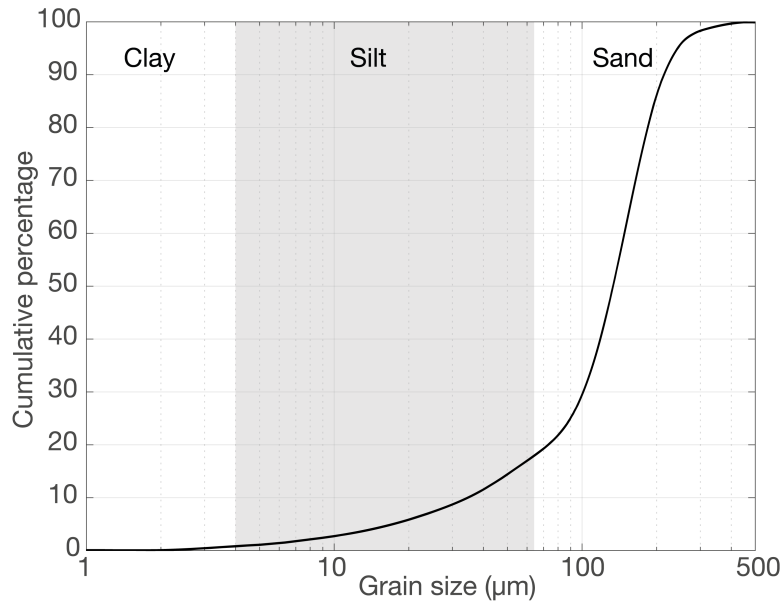
332 Fig. S7. Velocity measurements in the reference experiment.

333



334

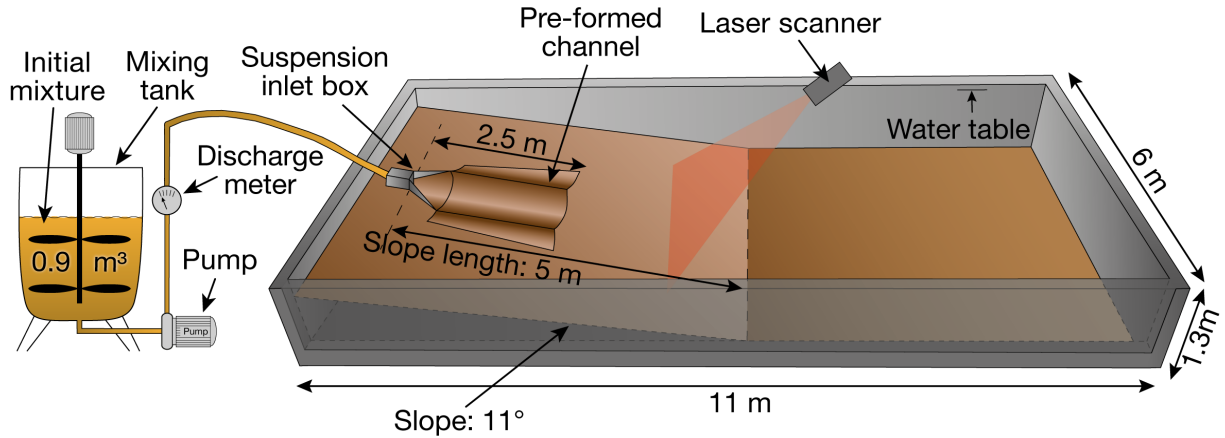
335 **Fig. S1. Shields mobility diagram.** Describes the dominant sediment transport mode for a  
 336 given set of hydrodynamic conditions. Modified after <sup>41</sup> and <sup>25</sup>. Natural flows were monitored  
 337 in the Monterey Canyon <sup>45</sup>, and the Congo Canyon <sup>2</sup>. For calculation of the point for the  
 338 Congo Canyon, the body of the current was used. Regime boundaries after: <sup>41,43,46,52,53</sup>



339

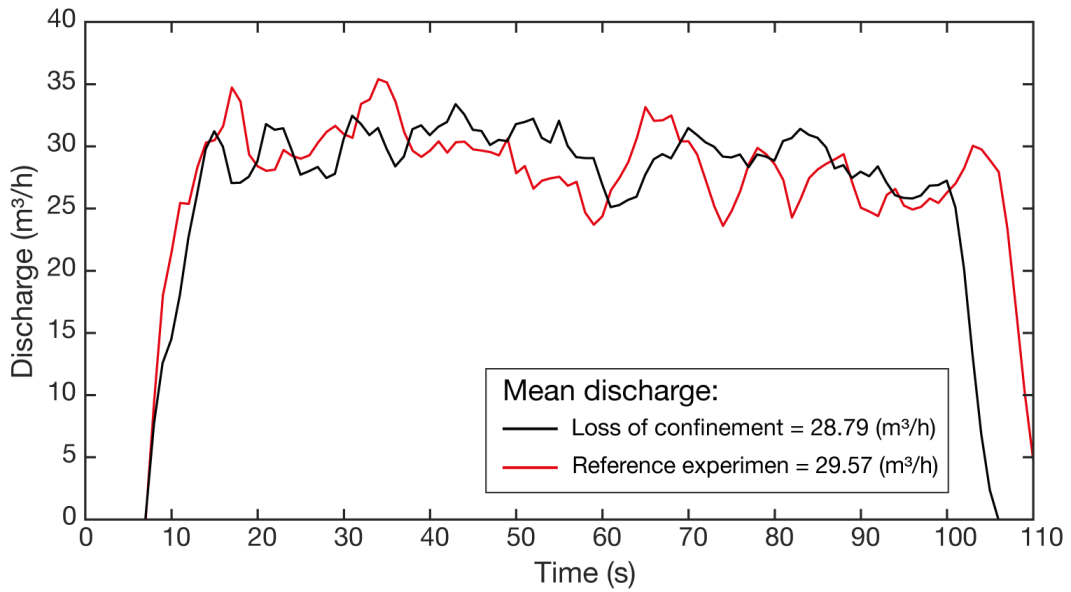
340 **Fig. S2. Cumulative grain-size distribution.** Sand of identical grain size was used for the  
 341 floor of the flume tank and for the suspended sediment of the turbidity current. Grain size was  
 342 measured with a laser particle sizer (Malvern Mastersizer 2000).

343



344

345 **Fig. S3 Schematic drawing of the experiment setup.** Note that the length of the reference  
 346 (no loss of confinement) experiment extended 5 m further downslope.



348 **Fig. S4. Discharge measurements of the two experiments.** The discharge was measured  
 349 with an electromagnetic flow-meter (Krohne Optiflux 2300). The mean discharge was  
 350 calculated by averaging over the time interval between 15 to 95 s.

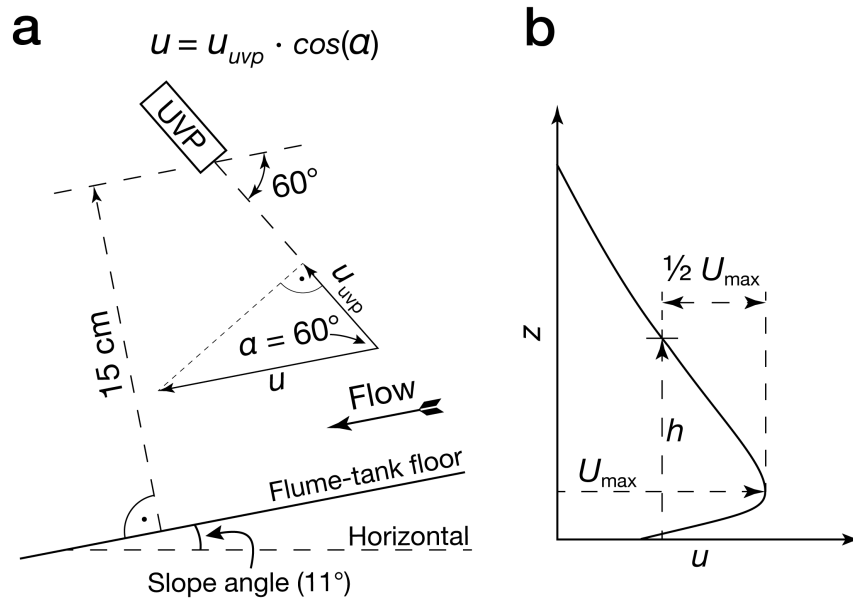
351

Manufacturer and type	MET-FLOW; DUO MX
Speed of sound in water (m/s)	1480
Measurement window (mm)	246.79
Number of channels	235
Distance between channel centers (mm)	0.925
Channel width (mm)	3.7
Frequency of the ultrasound beam (MHz)	1
Number of cycles per pulse	5
Number of sound pulses per measurement	32
Minimum on-axis velocity (mm/s)	-1081.9
Maximum on-axis velocity (mm/s)	1073.4
Velocity resolution (mm/s)	8.5
Time between each measurements (s)	1.247

352

353 **Tab. S1. UVP data acquisition settings.**

354

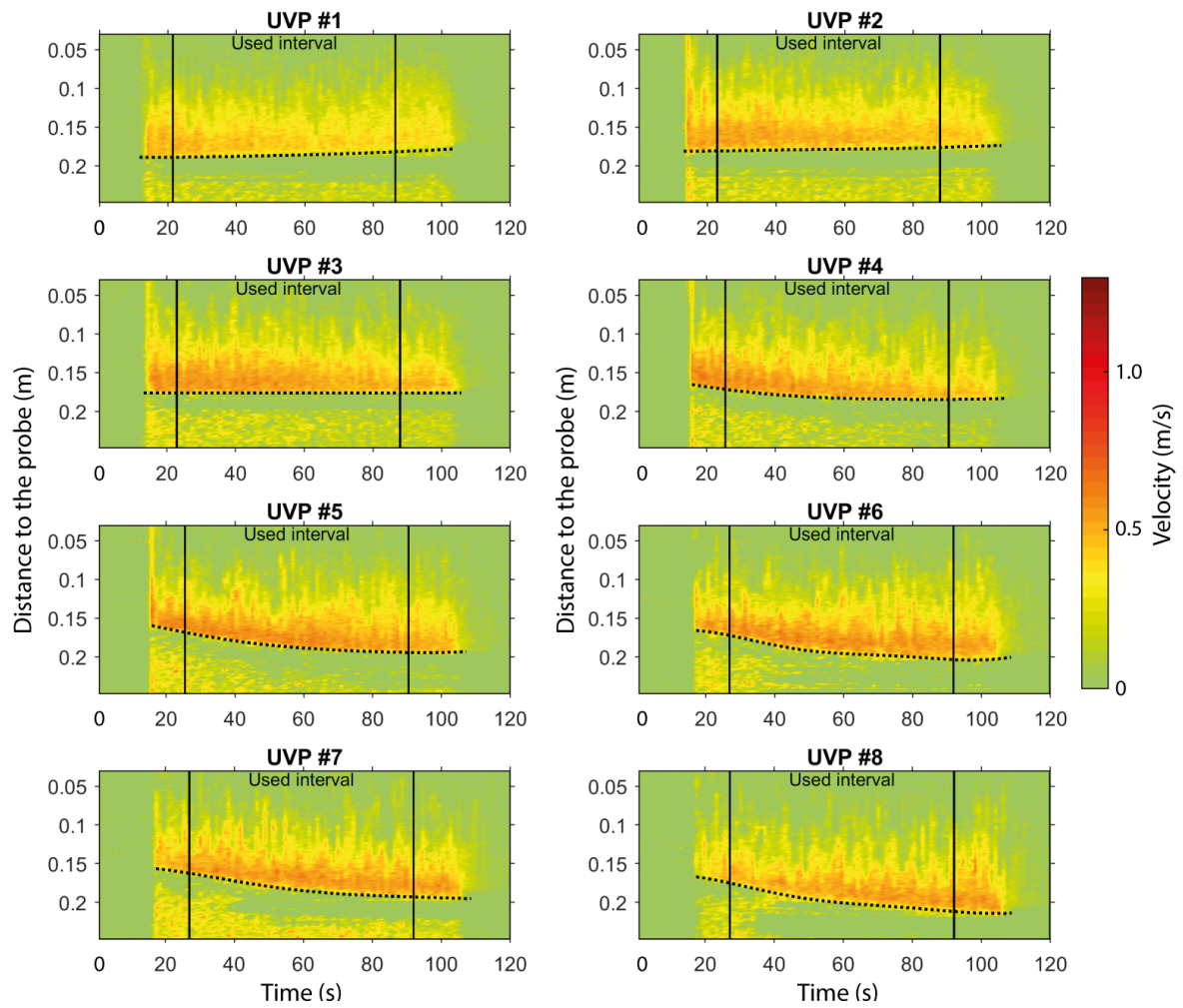


355

356 **Fig. S5. UVP orientation and parameterization of the velocity profile. a,b,** (a) The  
 357 orientation of the UVP and the trigonometric calculation to calculate bed-parallel velocities.  
 358  $u_{UVP}$  is the velocity component directed toward the UVP and  $u$  is the bed parallel velocity in  
 359 downflow direction. Not to scale. (b) Sketch of a velocity profile illustrating the analysis of  
 360 the time-averaged velocity profiles. Redrawn from <sup>50</sup>.

361

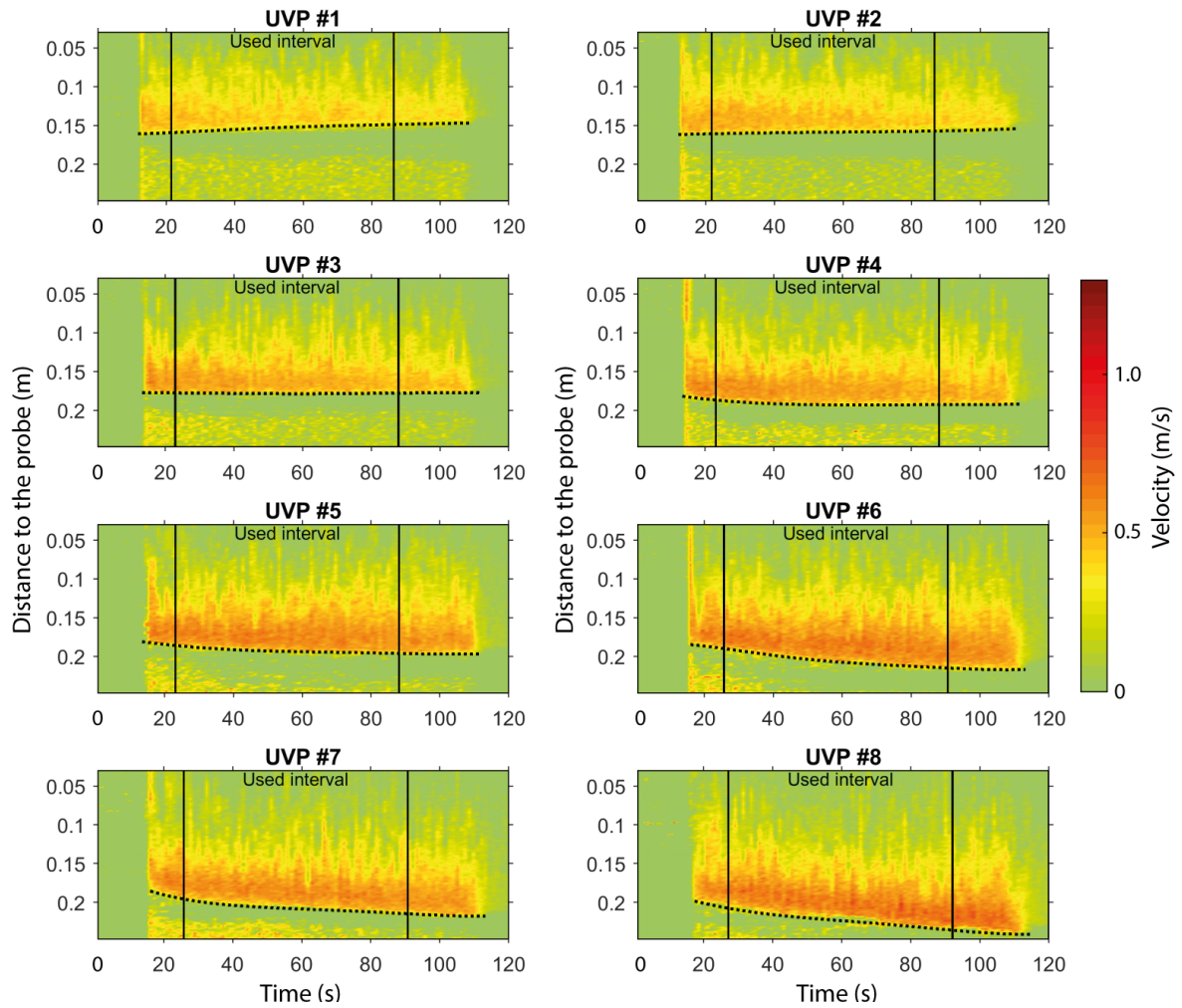




362

363 **Fig. S6. Velocity measurements in the experiment with loss of confinement.** The solid  
 364 vertical lines mark the interval that was used for analysis of the velocity data. The dashed line  
 365 indicated the position of the bed, where a sharp decrease in velocity occurs.

366



367

368 **Fig. S7. Velocity measurements in the reference experiment.** The solid vertical lines mark

369 the interval that was used for analysis of the velocity data. The dashed line indicated the

370 position of the bed, where a sharp decrease in velocity occurs.

371

372 **Author contributions**

373 J.T.E. and M.J.B.C. initiated the EuroSEDS project. F.P conducted the experiments,  
374 analysed the results and wrote the initial manuscript. All authors contributed to  
375 interpretation of the data and writing of the manuscript

376

377 **Competing interests statement**

378 The authors declare no competing interests.

## References

1. Galy, V. *et al.* Efficient organic carbon burial in the Bengal fan sustained by the Himalayan erosional system. *Nature* **450**, 407–410 (2007).
2. Azpiroz-Zabala, M. *et al.* Newly recognized turbidity current structure can explain prolonged flushing of submarine canyons. *Sci. Adv.* **3**, 1–12 (2017).
3. Nilsen, T. H., Shew, R. D., Steffens, G. S. & Studlick, J. R. J. *Studlick, Atlas of Deep-Water Outcrops.* (AAPG Studies in Geology 56 & Shell Exploration & Production. 504 pp., 2008).
4. Pham, C. K. *et al.* Marine litter distribution and density in European seas, from the shelves to deep basins. *PLoS One* **9**, 1–13 (2014).
5. Cressey, D. The Plastic Ocean. *Nature* **536**, 263–265 (2016).
6. Stevenson, C. J., Jackson, C. A.-L., Hodgson, D. M., Hubbard, S. M. & Eggenhuisen, J. T. Deep-Water Sediment Bypass. *J. Sediment. Res.* **85**, 1058–1081 (2015).
7. Bouma, A. H., Normark, W. R. & Barnes, N. E. *Submarine Fans and Related Turbidite Systems.* (Springer. 351 pp., 2012).
8. Mutti, E. & Normark, W. R. Comparing Examples of Modern and Ancient Turbidite Systems: Problems and Concepts. in *Marine Clastic Sedimentology* (eds. Leggett, J. K. & Zuffa, G. G.) 1–38 (Springer, 1987). doi:10.1007/978-94-009-3241-8\_1
9. Alexander, J. *et al.* Laboratory sustained turbidity currents form elongate ridges at channel mouths. *Sedimentology* **55**, 845–868 (2008).
10. Stacey, C. D. *et al.* How turbidity current frequency and character varies down a fjord-delta system: Combining direct monitoring, deposits and seismic data. *Sedimentology* **66**, 1–31 (2018).

11. Kenyon, N. H. & Millington, J. Contrasting deep-sea depositional systems in the Bering Sea. in *Atlas of Deep Water Environments* (eds. Pickering, K. T., Hiscott, R. N., Kenyon, N. H., Ricci Lucchi, F. & Smith, R. D. A.) 196–202 (Springer Netherlands, 1995).
12. Macdonald, H. A. *et al.* New insights into the morphology, fill, and remarkable longevity (>0.2 m.y.) of modern deep-water erosional scours along the northeast Atlantic margin. *Geosphere* **7**, 845–867 (2011).
13. Palanques, A., Kenyon, N. H., Alonso, B. & Limonov, A. Erosional and depositional patterns in the Valencia Channel mouth: An example of a modern channel-lobe transition zone. *Mar. Geophys. Res.* **18**, 104–118 (1996).
14. Wynn, R. B., Kenyon, N. H., Masson, D. G., Stow, D. A. V. & Weaver, P. P. E. Characterization and recognition of deep-water channel-lobe transition zones. *Am. Assoc. Pet. Geol. Bull.* **86**, 1441–1462 (2002).
15. Dorrell, R. M. *et al.* Flow dynamics and mixing processes in hydraulic jump arrays: Implications for channel-lobe transition zones. *Mar. Geol.* **381**, 181–193 (2016).
16. Yu, B. *et al.* Experiments on Self-Channelized Subaqueous Fans Emplaced by Turbidity Currents and Dilute Mudflows. *J. Sediment. Res.* **76**, 889–902 (2006).
17. Hodgson, D. M., Kane, I. A., Flint, S. S., Brunt, R. L. & Ortiz-Karpf, A. Time-Transgressive Confinement On the Slope and the Progradation of Basin-Floor Fans: Implications For the Sequence Stratigraphy of Deep-Water Deposits. *J. Sediment. Res.* **86**, 73–86 (2016).
18. Metivier, F., Lajeunesse, E. & Cacas, M.-C. Submarine Canyons in the Bathtub. *J. Sediment. Res.* **75**, 6–11 (2005).
19. Fildani, A. *et al.* Erosion at inception of deep-sea channels. *Mar. Pet. Geol.* **41**, 48–61

- (2013).
20. Hamilton, P. B., Strom, K. B. & Hoyal, D. C. J. D. Hydraulic and sediment transport properties of autogenic avulsion cycles on submarine fans with supercritical distributaries. *J. Geophys. Res. F Earth Surf.* **120**, 1369–1389 (2015).
  21. Komar, P. D. Hydraulic jumps in turbidity currents. *Bull. Geol. Soc. Am.* **82**, 1477–1488 (1971).
  22. Macdonald, R. G. *et al.* Flow patterns, sedimentation and deposit architecture under a hydraulic jump on a non-eroding bed: Defining hydraulic-jump unit bars. *Sedimentology* **56**, 1346–1367 (2009).
  23. Chanson, H. *Hydraulics of open channel flow*. (Elsevier. 650 pp., 2004).
  24. Russell, H. a J. & Arnott, R. W. C. Hydraulic-Jump and Hyperconcentrated-Flow Deposits of a Glacigenic Subaqueous Fan: Oak Ridges Moraine, Southern Ontario, Canada. *J. Sediment. Res.* **73**, 887–905 (2003).
  25. de Leeuw, J., Eggenhuisen, J. T. & Cartigny, M. J. B. Morphodynamics of submarine channel inception revealed by new experimental approach. *Nat. Commun.* **7**, 1–7 (2016).
  26. Eggenhuisen, J. T. & McCaffrey, W. D. Dynamic deviation of fluid pressure from hydrostatic pressure in turbidity currents. *Geology* **40**, 295–298 (2012).
  27. de Leeuw, J., Eggenhuisen, J. T. & Cartigny, M. J. B. Linking submarine channel–levee facies and architecture to flow structure of turbidity currents: insights from flume tank experiments. *Sedimentology* **65**, 931–951 (2018).
  28. Hofstra, M., Hodgson, D. M., Peakall, J. & Flint, S. S. Giant scour-fills in ancient channel-lobe transition zones: Formative processes and depositional architecture. *Sediment. Geol.* **329**, 98–114 (2015).

29. Garcia, M. & Parker, G. Experiments on hydraulic jumps in turbidity currents near a canyon-fan transition. *Science (80-. )*. **245**, 393–396 (1989).
30. Sumner, E. J. *et al.* First direct measurements of hydraulic jumps in an active submarine density current. *Geophys. Res. Lett.* **40**, 5904–5908 (2013).
31. Paull, C. K. *et al.* Powerful turbidity currents driven by dense basal layers. *Nat. Commun.* **9**, 4114 (2018).
32. Tilston, M., Arnott, R. W. C., Rennie, C. D. & Long, B. The influence of grain size on the velocity and sediment concentration profiles and depositional record of turbidity currents. *Geology* **43**, 839–842 (2015).
33. Sequeiros, O. E. *et al.* Characteristics of Velocity and Excess Density Profiles of Saline Underflows and Turbidity Currents Flowing over a Mobile Bed. *J. Hydraul. Eng.* **136**, 412–433 (2010).
34. Allen, J. R. L. Transverse erosional marks of mud and rock: their physical basis and geological significance. *Sediment. Geol.* **5**, 167–385 (1971).
35. Klauke, I., Hesse, R. & Ryan, W. B. F. F. Morphology and structure of a distal submarine trunk channel: The Northwest Atlantic Mid-Ocean Channel between lat 53°N and 44°30'N. *Bull. Geol. Soc. Am.* **110**, 22–34 (1998).
36. Jegou, I., Savoye, B., Pirmez, C. & Droz, L. Channel-mouth lobe complex of the recent Amazon Fan: The missing piece. *Mar. Geol.* **252**, 62–77 (2008).
37. Hughes Clarke, J. E. *et al.* The Squamish ProDelta : Monitoring Active Landslides and Turbidity Currents. *Can. Hydrogr. Conf. 2012* 1–15 (2012).
38. Straub, K. M. & Mohrig, D. Quantifying the morphology and growth of levees in aggrading submarine channels. *J. Geophys. Res. Earth Surf.* **113**, 1–20 (2008).
39. Brucker, S. *et al.* Monitoring flood-related change in bathymetry and sediment

- distribution over the Squamish Delta, Howe Sound, British Columbia. *U.S. Hydrogr. Conf.* 1–16 (2007).
40. Zhong, G., Cartigny, M. J. B., Kuang, Z. & Wang, L. Cyclic steps along the South Taiwan Shoal and West Penghu submarine canyons on the northeastern continental slope of the South China Sea. *Bull. Geol. Soc. Am.* **127**, 804–824 (2015).
  41. Shields, A. Anwendung der Aehnlichkeitsmechanig und der Turbulenzforschung auf die Geschiebebewegung. *Mitteilungen der Preußischen Versuchsanstalt für Wasserbau und Schiffbau* **26**, (Technische Hochschule Berlin, 25 pp, 1936).
  42. Middleton, G. V & Southard, J. B. *Mechanics of Sediment Movement*. **3**, (SEPM, Eastern Section Short Course 3 Providence, 401 pp., 1984).
  43. van Rijn, L. C. *Principles of sediment transport in rivers, estuaries and coastal seas*. *Aqua publications* (Aqua publications. 790 pp., 1993). doi:10.1002/9781444308785
  44. Cartigny, M. J. B., Eggenhuisen, J. T., Hansen, E. W. M. & Postma, G. Concentration-Dependent Flow Stratification In Experimental High-Density Turbidity Currents and Their Relevance To Turbidite Facies Models. *J. Sediment. Res.* **83**, 1046–1064 (2013).
  45. Xu, J. P. Normalized velocity profiles of field-measured turbidity currents. *Geology* **38**, 563–566 (2010).
  46. Garcia, M. *Sedimentation Engineering: Processes, Measurements, Modeling and Practise*. *Am. Soc. Civ. Eng.* 1132 pp. (2008).
  47. Xu, J. P., Sequeiros, O. E. & Noble, M. A. Sediment concentrations, flow conditions, and downstream evolution of two turbidity currents, Monterey Canyon, USA. *Deep. Res. Part I Oceanogr. Res. Pap.* **89**, 11–34 (2014).
  48. Buckee, C., Kneller, C. & Peakall, J. Turbulence structure in steady, solute-driven gravity currents. in *Particulate gravity currents* (eds. Mccaffrey, W. D., Kneller, B. &



- Peakall, J.) 173–188 (International Association of Sedimentologists, Special Publication 31, Blackwell Science, 2001).
49. Kneller, B. & Buckee, C. The structure and fluid mechanics of turbidity currents: a review of some recent studies and their geological implications. *Sedimentology* **47**, 62–94 (2000).
  50. Launder, B. E. & Rodi, W. The Turbulent Wall Jet Measurements and Modeling. *Annu. Rev. Fluid Mech.* **15**, 429–459 (1983).
  51. Gray, T. E., Alexander, J. & Leeder, M. R. Quantifying velocity and turbulence structure in depositing sustained turbidity currents across breaks in slope. *Sedimentology* **52**, 467–488 (2005).
  52. Bagnold, R. A. *An Approach to the Sediment Transport Problem from General Physics*. USGS Professional Paper 422-1 (USGS Professional Paper 422-1, U.S. Government Printing Office, 1966). doi:10.1017/S0016756800049074
  53. Nino, Y., Lopez, F. & Garcia, M. Threshold for particle entrainment into suspension. *Sedimentology* **50**, 247–263 (2003).